



Phase field modeling of ductile fracture at large plastic strains using adaptive isotropic remeshing

Hazem Eldahshan^{1,2} · Pierre-Olivier Bouchard¹ · José Alves² · Etienne Perchat² · Daniel Pino Munoz¹

Received: 16 March 2020 / Accepted: 1 December 2020 / Published online: 11 January 2021
© The Author(s), under exclusive licence to Springer-Verlag GmbH, DE part of Springer Nature 2021

Abstract

In this paper, a phase field model of ductile fracture is described within the framework of large plastic strains. Most results dealing with phase field modeling of ductile fracture are carried out on a fixed mesh, which requires a fine mesh throughout all the computation. The aim of this paper is to introduce an adaptive isotropic remeshing strategy coupled with a phase field model of ductile fracture to achieve accurate results with a major decrease in computational time. A mixed velocity/pressure finite element formulation is used for the solution of mechanical fields. The plastic strain field needs to be transferred to the new mesh after each remeshing operation. This field transfer requires the use of a suitable remeshing-transfer operator. Different field transfer operators are tested and results are reported. In order to reduce the numerical diffusion associated with the field transfer operation, a volume quality based metric has been introduced. This paper presents different numerical examples with both qualitative and quantitative analyses in order to show the ability of the developed strategy in predicting crack evolution in ductile materials. The proposed framework is also able to predict crack paths in highly ductile materials while benefiting from space-adaptivity.

Keywords Phase field model · Ductile fracture · Velocity/pressure finite element · Adaptive isotropic remeshing · Field transfer operator

1 Introduction

The phase field model for fracture was introduced in a variational form by Francfort and Marigo [1] as a generalization of Griffith's criterion to predict the critical stress for brittle fracture. The minimization of a functional that contains the sum of total elastic strain energy and fracture energy enables predicting the initiation, propagation, merging and branching of multiple cracks under complex loading conditions. Nonetheless, the original formulation is not appropriate for numerical treatment since the crack surfaces are not known a priori; hence the computational scheme becomes non-tractable in the sense that the resulting algorithm will be complicated to implement. Fortunately, this problem has been tackled in the

field of image processing with the so-called Mumford-Shah functional [2] and thereafter a regularization introduced by Ambrosio and Tortorelli [3]. Bourdin et al. [4] introduced a numerical procedure based on the regularized functional that substitutes the sharp crack topology by a damaged zone with a field variable known as “phase field” that goes from 0 (intact material) to 1 (totally damaged).

Most of the phase field models available in the literature deal with the problem of brittle fracture [5–7]. However, many extensions of the phase field model for ductile fracture have been introduced in the literature for 2D configurations [8,9] and also for 3D configurations with finite strains [9–13]. Recently, a porous-ductile phase field model was introduced in [14] in which the critical energy release rate is decomposed into elastic and plastic parts where the plastic deformation is described by a modified GTN model [15,16]. Unfortunately, the phase field model for ductile fracture is not variationally consistent. In consequence, different options are proposed in the literature on the way plastic strains can contribute to the ductile fracture in order to mimic the behaviour of brittle fracture. For example, Ambati et al. [8] introduced a new degradation function that contains the equivalent plastic

✉ Hazem Eldahshan
hazem.eldahshan@mines-paristech.fr

¹ MINES Paris-Tech, PSL- Research University, CEMEF - Center for Material Forming, CNRS UMR 7635, BP 207, 1 rue Claude Daunesse, 06904 Sophia Antipolis Cedex, France

² Transvalor SA, E-Golf Park, 950 Avenue Roumanille, 06410 Biot, France

strain in an exponential form. This means that the material is degraded in regions where the plastic strain is localized; hence the crack propagation is directly affected by plasticity. On the other hand, Borden et al. [11] added the plastic strain energy along with a plastic degradation function that depends only on the phase field variable in the crack driving force. A good review for the different phase field models of ductile fracture can be found in [17].

In the current work, the model of Borden [11] is implemented in **FORGE**®¹ where a mixed velocity/pressure finite element model with a bubble function stabilization known as P1+/P1 is used to solve the mechanical equations using tetrahedral elements. The bubble stabilization technique is used in order to satisfy the Brezzi-Babuska inf-sup condition [18,19]. The resulting finite element model is able to solve the mechanical problems with large plastic strains while minimizing numerical instabilities. The phase field equation is solved on the same mesh. A staggered algorithm is used to decouple the solution of mechanical equations from the phase field equation since the resulting coupled system of equations is highly nonlinear [6]. Numerical comparisons are carried out in order to validate the current numerical implementation with the original model.

Starting the computations with a fixed mesh that is locally refined in the areas where the phase field is expected to propagate is the main strategy used in the literature to solve this problem. It can be expected that two problems emerge when this strategy is applied: (i). the locations of cracks need to be known a priori which is not the case in most of the applications in fracture mechanics; (ii). the number of elements in the mesh becomes very large from the beginning of the computations which is usually not needed before a crack is initiated, hence the computational scheme becomes inefficient. In order to deal with these problems, an adaptive isotropic remeshing strategy is used in order to adapt the mesh in the regions where the phase field is expected to propagate. In isotropic remeshing, all edges of each element should be scaled with the same multiplicative factor which is suitable for our purpose. Very few attempts to use adaptive remeshing strategies coupled with a phase field model in the context of brittle fracture have been reported in the literature. To the extend of our knowledge, the development of an adaptive remeshing scheme for the phase field model for ductile fracture has not been addressed before in the literature.

A multi-scale modeling approach has been adopted in [20] to keep a small mesh size around the crack tip. A fine mesh structure is defined with respect to a coarse mesh topology using a multi scale basis functions.

Another proposition of a multi level hp-FEM strategy has been adopted also in [21] for brittle fracture simulations.

They showed that with the developed remeshing strategy, it was possible to obtain accurate numerical results as compared to the cases with a fixed mesh. The main advantage is the great reduction in the number of degrees of freedom at the beginning of the simulation and hence the computational time decreases significantly. In [22], a predictor-corrector refinement strategy inspired by the work in [23] is presented within a global-local approach for the anisotropic phase field modeling. The solution of the mechanical system is solved on a global coarse mesh while the phase field solution is based on a local refined mesh. Recently, Alba Muixi et al. [24] introduced a new h-refinement strategy that is based on the use of two types of elements: standard and refined elements where continuity is imposed in a weak sense by the means of Nitsche's method. In addition, Patil et al. [25] presented a Phase field adaptive scheme for brittle materials that combines three different methods: (i). Phase field method; (ii). Extended finite element method (XFEM); (iii). Multiscale finite element method. The proposed approach reduces the solution domain to a small vicinity around the crack tip with an adaptive refinement which reduces significantly the computation time.

In [26], a predictor-corrector remeshing strategy is implemented within the framework of brittle fracture. Starting with a coarse mesh, a two-steps solution procedure is adopted: a predictor step on a coarse mesh is first used to obtain initial results which is followed by a refinement step where the solution is recalculated. A similar idea is used in [23], a solution is obtained at time t on an initial mesh. Then, the time advances and if the crack is found to propagate outside the refined zone, a refinement operation takes place while the old phase solution is interpolated on the new mesh. The process is repeated until no change happens.

Authors in [27] introduced a computational framework known as VEM (Virtual element method) as a generalization of the classical finite elements method that can be used to form any shape of elements with an arbitrary number of nodes. The developed method is suitable for crack propagation and brittle and ductile fracture simulations [28,29]. Ali Hussein et al. [30] introduced an adaptive crack simulation framework using the phase field method and the VEM in brittle materials. The mesh is refined around the crack tip when the maximum value of the phase field reaches some threshold which is followed by an equilibrium step using the staggered algorithm. Finally, a cutting algorithm is used to split the virtual elements and open the crack faces.

In this paper, we generalize the remeshing operation to deal with ductile fracture where the material is history dependent due to plastic deformations. Three main challenges are to be studied: (i). the choice of an appropriate refinement indicator function that is suitable for ductile materials; (ii). the choice of a conservative field transfer operator that minimizes the numerical diffusion during the transport of fields;

¹ FORGE® is a finite element software specialized in material forming simulation.

(iii). the reduction of the number of remeshing operations in order to minimize the numerical diffusion that could lead to inaccurate tracking for the crack path. The ultimate goal is to have a numerical framework that is able to accurately resolve the phase field equations while reducing the computational time in ductile fracture simulations. A comprehensive review for the different field transfer operators can be found in [31]. The paper is structured as follows: Sect. 2 introduces the variational formulation of the phase field method for ductile fracture within the framework of velocity/pressure mixed finite element formulation. Then Sect. 3 presents the adaptive isotropic remeshing scheme used in this work. In Sect. 4, two numerical examples are presented with both qualitative and quantitative analyses. Finally, a conclusion with some perspectives on the future work is drawn in Sect. 5.

2 Formulation of the problem

2.1 Original formulation

The first step is to define a free energy functional \mathcal{E} which is a Mumford-Shah [2] type as follows

$$\mathcal{E}(\mathbf{u}, \Gamma) = \int_{\Omega_h} W_e(\boldsymbol{\varepsilon}^e) d\Omega_h + \int_{\Gamma} G_c d\Gamma \tag{1}$$

where $\boldsymbol{\varepsilon}^e$ is the elastic strain tensor, W_e is the elastic energy density, G_c is the fracture toughness, Ω_h is the occupied volume in the reference configuration (Fig. 1a) and Γ is the crack surface in the reference configuration. This energy functional is an extension of the Griffith’s definition of brittle fracture. The competition between internal elastic and fracture energies leads to the onset and propagation of cracks in materials. As can be observed, it is needed to determine a priori the fractured surface in order to calculate the fracture energy. This results in a computational scheme that is non-tractable and inconvenient to apply. To facilitate the solution of this problem, another variational formulation based on regularizing the energy functional following the work of Ambrosio and Tortorelli was introduced [3]. With this approximation, a scalar variable known as the phase field variable is added; d goes from 0 (intact material) to 1 (totally broken) (Fig. 1b). The variational formulation of *brittle diffused damage* is written as

$$\mathcal{E}_l(\mathbf{u}, d) = \int_{\Omega_h} g_e(d) W_e(\boldsymbol{\varepsilon}^e) d\Omega_h + \int_{\Omega_h} G_c \mathcal{C}(d, \nabla d) d\Omega_h \tag{2}$$

where two new components are added:

$g_e(d)$ is an elastic degradation function that is defined as follows

$$g_e(d) = ((1 - d) + \zeta)^2 \tag{3}$$

and $\mathcal{C}(d, \nabla d)$ is the crack surface density that diffuses the sharp crack topology into a continuous field

$$\mathcal{C}(d, \nabla d) = \frac{1}{2l_c} (d^2 + l_c^2 |\nabla d|^2) \tag{4}$$

where ζ is a numerical parameter used to prevent the singularity of the stiffness matrix. Minimizing the regularized energy functional would give a differential equation that governs the evolution of the phase field in brittle materials. Miehe et al. [6,32] proposed a thermodynamically consistent formulation to the phase field problem based on transforming the discontinuous nature of the crack to a continuous one leading to very similar mathematical formulation.

In order to deal with the ductile fracture problems, new components should be added to the formulation such as plastic strain, stress triaxiality and lode parameter [33]. M. Ambati et al. [8] showed that although there is no variationally consistent formulation for the phase field problem of ductile fracture, it is possible to mimic the brittle fracture formulation by adding components that represent the ductility of the material. Authors proposed to couple the elastic degradation function with the equivalent strain through an exponential form. In addition, Borden et al. [11] added the plastic energy with a new plastic degradation function to the free energy functional.

2.2 Phase field formulation of ductile fracture

Following the work of [11], the plastic strain energy is added to the crack driving force \mathcal{H} where a plastic degradation function g_p is added in order to weaken the material where the plastic deformation is localized. The strong form of the phase field evolution equation is written as

$$\frac{G_c}{l_c} (d - l_c^2 \nabla^2 d) = \mathcal{H}(\underline{\mathbf{x}}, t) \text{ (Evolution of the phase field)} \tag{5a}$$

$$\mathcal{H} = \beta_1 g'_e(d) \max_n W_e(\boldsymbol{\varepsilon}^e(\underline{\mathbf{x}}, d_n)) + \beta_2 g'_p(d) < W_p(\bar{\boldsymbol{\varepsilon}}) - W_0 > \text{ (Crack driving force)} \tag{5b}$$

$$\nabla d \cdot \mathbf{n} = 0 \text{ (Neumann boundary condition)} \tag{5c}$$

the angle bracket operator is defined as follows:

$$< x > = \begin{cases} x & x \geq 0 \\ 0 & x < 0 \end{cases}$$

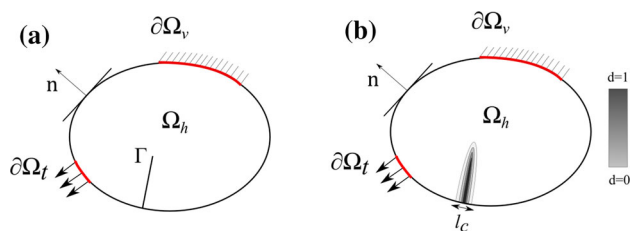


Fig. 1 **a** Geometry and boundary conditions of an arbitrary domain with discontinuity Γ . **b** Transformation of the crack to a diffused damage with the phase field d that goes from 0 to 1

$\bar{\epsilon}$ is the equivalent plastic strain, d is the phase field variable that varies from 0 (intact material) to 1 (totally broken), W_e is the elastic strain energy, W_p is the equivalent plastic strain energy, \mathcal{H} is the crack driving force, g_e and g_p are the elastic and plastic degradation functions, respectively. For simplicity, the plastic degradation function g_p is chosen to be the same as the elastic one represented in Eq. 3 as used in [11]. G_c is the fracture toughness, l_c is a predefined length scale, β_1, β_2 and W_0 are numerical parameters used for calibrating the phenomenological model and \mathbf{n} is a unit vector normal to the surface. The Neumann boundary condition is imposed to ensure that no external source can actively create the crack. In other words, the crack evolution is governed by the evolution of other mechanical fields (Fig. 1).

2.3 Mechanical behaviour at large strains

Two main formulations are used in order to deal with large strain nonlinear problems within the context of finite element analysis: (i). Total lagrange formulation; (ii). Updated lagrange formulation [34,35]. In order to deal with the problem of large plastic strains, an updated lagrangian formulation coupled with adaptive remeshing is used. With the updated lagrange formulation, the new reference configuration is set to be the deformed configuration of the last time step. In consequence, a continuous update of the geometry coordinates necessitates adaptive remeshing operation in order to conserve the quality of elements used throughout the simulation.

2.4 Mechanical constitutive law

An elasto-plastic constitutive material law is considered. Applying the phase field model without any special treatment for crack evolution in the regions where compressive stresses exist have shown unrealistic interpenetration of crack lips. Bourdin et al. have already demonstrated with numerical examples in [4] this problem.

2.4.1 Elastic model

Decomposing the elastic strain energy into positive and negative parts while degrading solely the positive part seems to solve the aforementioned problem. The final form of the elastic energy can be decomposed as

$$W_e(\boldsymbol{\epsilon}^e) = g_e(d)W_e^+(\boldsymbol{\epsilon}^e) + W_e^-(\boldsymbol{\epsilon}^e) \tag{6}$$

where W_e^+ and W_e^- are the positive and negative parts of the elastic strain energy, respectively.

The approach introduced by Amor et al. [36] for the energy decomposition is used as follows:

$$\begin{aligned} W_e^+(\boldsymbol{\epsilon}^e, d) &= \frac{\kappa}{2} \langle \text{tr}(\boldsymbol{\epsilon}^e) \rangle_+^2 + \mu \boldsymbol{\epsilon}_{dev}^e : \boldsymbol{\epsilon}_{dev}^e \\ W_e^-(\boldsymbol{\epsilon}^e, d) &= \frac{\kappa}{2} \langle \text{tr}(\boldsymbol{\epsilon}^e) \rangle_-^2 \end{aligned} \tag{7}$$

where $\boldsymbol{\epsilon}_{dev}^e = \boldsymbol{\epsilon}^e - \frac{\text{tr}(\boldsymbol{\epsilon}^e)}{3} \mathbf{1}$, $\mu = \frac{E}{2(1+\nu)}$, E is the Young’s modulus, ν is Poisson’s ratio and κ is the bulk’s modulus.

where

$$\langle x \rangle_+ = \begin{cases} x & x \geq 0 \\ 0 & x < 0 \end{cases} \quad \langle x \rangle_- = \begin{cases} 0 & x \geq 0 \\ x & x < 0 \end{cases}$$

The first part of the positive elastic strain energy W_e^+ replaces the total strain energy W_e that appears in Eq. 5b. The positive elastic energy W_e^+ contains a volumetric part that reflects the effect of dilatation along with the deviatoric part that reflects the effect of shear deformation. The positive elastic strain energy enters in competition with the fracture energy resulting in the evolution of the phase field.

On the other hand, the negative part of the elastic energy density that is related to reduction in volume does not contribute to the evolution of the phase field.

The resulting constitutive relation is shown as

$$\boldsymbol{\sigma} = \kappa(1 - \alpha d)^2 \text{tr}(\boldsymbol{\epsilon}^e) \mathbf{1} + 2(1 - d)^2 \boldsymbol{\epsilon}_{dev}^e I^{dev} \tag{8}$$

where

$$\alpha = \begin{cases} 1 & \text{tr}(\boldsymbol{\epsilon}^e) > 0 \\ 0 & \text{else} \end{cases}$$

and $I_{ijkl}^{dev} = I_{ijkl} - \frac{1}{3} \delta_{ij} \delta_{kl}$, $I_{ijkl} = \frac{1}{2} (\delta_{ij} \delta_{kl} + \delta_{ik} \delta_{jl})$ with δ the Kronecker’s delta.

2.4.2 Elasto-Plastic model

The return mapping algorithm is used to update the equivalent plastic strain and deviatoric Cauchy stress tensor at

each time step, with the assumption of no plastic deformation increment, the resulting equations can be written as

$$s^{trial} = 2\mu g_e(d_n) [\boldsymbol{\epsilon}_{n+1} - \boldsymbol{\epsilon}_n^p] \tag{9a}$$

$$f^{trial} = \sigma_{VM} - g_p(d_n)\sigma_0(\bar{\boldsymbol{\epsilon}}_n) \leq 0 \tag{9b}$$

where

$$\sigma_{VM} = \sqrt{3 J_2(s_{n+1}^{trial})} \tag{10}$$

where s^{trial} is the trial deviatoric stress, $\boldsymbol{\epsilon}$ is the total strain tensor and $\boldsymbol{\epsilon}^p$ is the plastic strain tensor, J_2 is the second invariant of the deviatoric stress tensor and n is the increment number. If condition 9b is not satisfied, a new plastic deformation increment is found as follows

$$f = \sqrt{3 J_2(s_{n+1}^{trial})} - g_p(d_n)\sigma_0(\bar{\boldsymbol{\epsilon}}_{n+1}) - 3\mu g_p(d_n)\Delta\lambda = 0 \tag{11}$$

where λ is the plastic multiplier. The effective stress is defined as follows

$$\sigma_0 = \sigma_y + H\bar{\boldsymbol{\epsilon}} \tag{12}$$

where σ_y is the initial yield stress and H is the plastic modulus. It should be noted that d_n is constant in Eq. 11. A Newton-Raphson nonlinear solver is used to solve Eq. 11, the plastic strain update is written as

$$\bar{\boldsymbol{\epsilon}}_{n+1} = \bar{\boldsymbol{\epsilon}}_n + \Delta\lambda \tag{13}$$

The update of the deviatoric stress tensor and discrete tangent modulus are expressed as follows

$$s_{n+1} = \frac{s_{n+1}^{trial}}{1 + \frac{3\mu g_e(d_n)\Delta\lambda}{\sigma_0(\bar{\boldsymbol{\epsilon}}_{n+1})}} \tag{14}$$

$$C_{n+1}^d = \frac{\partial \dot{s}^{n+1}}{\partial \dot{\boldsymbol{\epsilon}}^{n+1}} = 2\mu g_e(d_n) \left(1 - 6 \frac{\mu^2 \Delta\lambda}{J_2(s_{n+1}^{trial})} \mathbf{I}^{dev} \right) - 4\mu^2 \bar{\mathbf{n}} \otimes \bar{\mathbf{n}} \left(\frac{1}{\frac{\partial \sigma_0}{\partial \bar{\boldsymbol{\epsilon}}} + 3\mu g_e(d_n)} + \frac{\Delta\lambda}{J_2(s_{n+1}^{trial})} \right) \tag{15}$$

where $\bar{\mathbf{n}} = \frac{3}{2} \frac{s}{J_2(s_{n+1})}$ and \otimes is the tensor product.

3 Adaptive isotropic remeshing

The most used strategy in the literature to deal with the phase field model is to use a fixed mesh with local refinement. The minimum element size h_{min} should be chosen in order to properly describe the damage zone. However, a larger element size can be used at the beginning of the simulation

before starting the damage initiates. As recommended by Miehe et al. [6], h_{min} in the critical zones where the crack is expected to propagate is chosen to be two times less than the length scale l_c . Two main problems arise with that choice: (i). the element size is not necessary to get accurate results before damage occurs, which leads to high unnecessary computational cost; (ii). the fact that the mesh size should be refined before starting the computations contradicts the purpose of our model which is to predict the location of crack initiation and propagation.

In this article, an adaptive scheme is adopted to generate new meshes that are refined in the regions where the phase field is expected to propagate. The originality of the current work comes from the applicability of the developed tools to deal with both brittle and ductile fracture patterns using the phase field model. Three main challenges exist with the adopted remeshing strategy: (i). controlling the number of remeshing operations until the final geometry is obtained; (ii). the choice of an indicator function that triggers the remeshing process; (iii) the choice of a consistent field transfer operator that minimizes the numerical diffusion after each remeshing step.

Elements are refined upon reaching a given threshold for a given indicator function that can be tailored numerically. A tag for each element is used to know whether or not it needs to be refined during the computations.

3.1 Controlling the number of remeshing operations

Numerical diffusion during remeshing is inevitable. Thus, the solution will be more conservative as the number of remeshing operations is reduced. Once a sufficiently refined mesh is obtained, the remeshing process should be terminated. In order to achieve that objective, another indicator function is proposed that is based on a volume quality metric. The volume quality metric is defined as the ratio between the new and old volumes of each element. At each increment, the new volume of each element is calculated based on the nodal values of the phase field. For example, if the smallest volume quality among all elements of the new mesh exceeds a given threshold, a remeshing step is carried out. Otherwise, no remeshing step is done. Figure 2 illustrates the way of calculating the element size. The size related to the phase field value at each node is determined based on the value of the phase field, i.e., the size only changes if the phase field value exceeds the pre-set threshold. At each increment, a volume quality metric \mathcal{B} is calculated for each element T as follows

$$\mathcal{B}(T) = \min\left(\left(\frac{l_{new}}{l_{old}}\right)^3, \left(\frac{l_{old}}{l_{new}}\right)^3, \frac{V_{\Omega_1}}{V_{Ref}}\right) \tag{16}$$

where l_{new} is the average length of a tetrahedron in the new mesh in case of remeshing, l_{old} is the average length of a

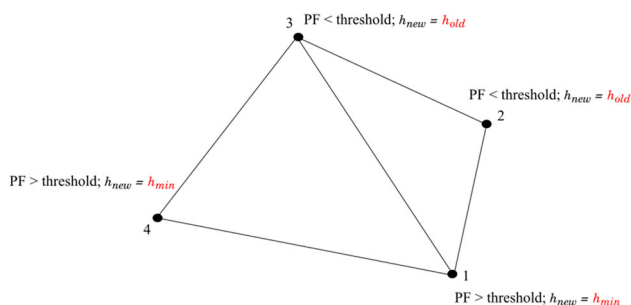


Fig. 2 Calculating the new element size based on the phase field values at the nodes

tetrahedron in the old mesh, V_{Ω_1} is the volume of a tetrahedron in the old mesh and V_{Ref} is the volume of a reference equilateral element of the same average length as the element of the new mesh in case of remeshing.

The mesh quality threshold can be chosen to be as follows

$$\text{Mesh quality threshold} = \left(\frac{l_f}{\eta l_0}\right)^3 \quad (17)$$

where l_f is the pre-set element size in the refined zone in which the phase field is expected to propagate, l_0 is the element size of the initial mesh and η is a numerical parameter that varies between 0.6 and 1.4. This artificial parameter η gives some tolerance for the remeshing initiation process as the initial element size distribution is heterogeneous. The proposed threshold gives an upper bound for the ratio of element volume between the old and new meshes.

This proposed mesh quality metric is essential in limiting data diffusion due to remeshing. In other words, the rule here is that: once the region in which the crack is expected to propagate is remeshed, the remeshing is terminated.

3.2 Field transfer operator

Field transfer operation refers to the transport of fields between two different topologies representing the same geometrical space. Regardless of the method used in this step, an amount of data is always lost due to the non-exact transfer of fields. The main features of a conservative remeshing-transfer operator are: (i). Minimizing the numerical diffusion; (ii). Preserving the mechanical equilibrium. Two types of fields can be transferred, nodal fields and fields that are stored at the integration points. For the updated lagrangian formulation that is used in this study, both the nodal fields and the fields that are stored at the integration points will be interpolated to the new mesh.

Two categories of transfer operator will be used for the sake of demonstration: (i). P0 transfer: each integration point in the new mesh takes the value of its nearest neighbourhood in the old mesh; (ii) P1 transfer: A three-step procedure is

carried out (i). A smoothing operator transforms the field stored at the integration points to a nodal field; (ii). A direct interpolation maps the nodal fields of the old mesh to the new mesh; (iii). The continuous field at the new mesh is remapped to the integration points [37,38].

Different remeshing transfer operators are introduced in the literature. Sushil Kumar et al. [31] presented a comparison between a wide categories of methods related to the recovery by element patches and recovery by nodal patches. Authors have shown that increasing the interpolation order of the transfer operator increased the accuracy and convergence behaviour by the same order. In [39], a continuous solution is given in the vicinity of a given integration point that is considered to be valid for a patch of elements. Then, the value is used for the element of the new mesh that contains this integration point. Likewise, Zienkiewicz and Zhu presented in [40] the SPR (Super convergent Patch Recovery) method which is based on retrieving a mapped stress field using a patch of elements sharing a common node. In order to ensure the equilibrium after each remeshing operation, a few Newton-Raphson iterations need to be carried out as suggested in [41]. Authors in [42] propose to divide the loading step just after the remeshing operation to two steps in order facilitate the convergence while ensuring the equilibrium. Another proposition in [31,43] is to ensure that the transferred field preserves the equilibrium at the new mesh.

In this article, for the sake of simplicity, two field transfer operators are tested: i. Nearest point interpolation method; ii. P1 transfer by Galerkin smoothing method.

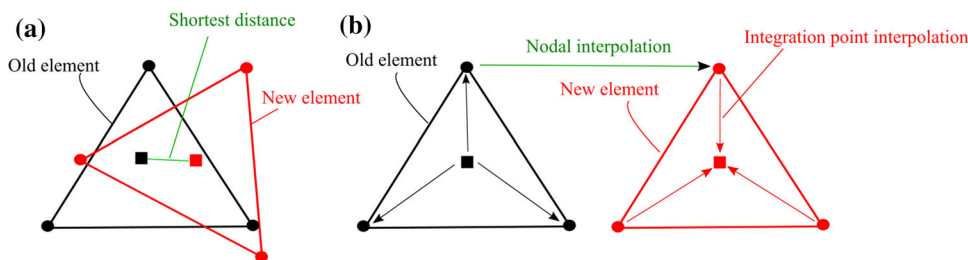
3.2.1 P0 transfer method (Nearest point interpolation)

This method is the simplest one among the other field transfer operators. However, it lacks a proper mathematical consistency when compared to other methods so that it can be very diffusive if the mesh is not very refined. The values of P0 fields (constant per element) are transferred directly from each integration point of the old mesh to the nearest new point in the new mesh as shown in Fig. 3a. This technique has the advantage of preserving the values of the transferred field when the changes in the mesh topology are very small. However, the remapping error is proportional to the field gradient, i.e., when the gradient of a given field is very high, it becomes very difficult to recover the fields with high accuracy. This technique also has the advantage of a low computational cost since no additional operations are done except for locating the nearest neighbourhood of each integration point in the mesh. Figure 3a summarizes the steps of this method.

3.2.2 P1 transfer with Galerkin smoothing

The Galerkin smoothing method is referred to the smoothing of discontinuous P0 fields in order to build another continu-

Fig. 3 Field interpolation method: **a** P0 transfer (Nearest point interpolation). **b** P1 transfer with Galerkin smoothing



ous P1 field per element. This means that at each time step the P0 fields are transformed to be P1 fields followed by a direct nodal interpolation using the same interpolation functions used for the finite element solution as shown in Fig. 3b. Finally, a P0 field is recovered from the constructed P1 field. The main advantage of this method is that it is expected to be more conservative than the nearest point interpolation method when the old and new mesh typologies are very different. On the contrary, it should always be expected to have an amount of data loss due to the P0-P1-P0 transformations even if the mesh topological changes are small.

Let us consider a given discontinuous field g_{P0} that is calculated on an old mesh and the new continuous field calculated at the element nodes f_{P1} . Recovering the same field at the nodes requires that

$$f_{P1} = g_{P0} \tag{18}$$

since the condition cannot be strongly applied due to the nature of the two functions, transforming the equation into a weak form and minimizing the residual using the Galerkin smoothing method would be a possible solution. The weak form applied over an element gives

$$\int_{\Omega_h} \phi_h f_{P1} d\Omega = \int_{\Omega_h} \phi_h g_{P0} d\Omega \tag{19}$$

where ϕ_h is a test function. The functions f_{P1} and ϕ_h are defined as follows

$$f_{P1} = \sum_{k=1}^{N_n} N_i^k \hat{f}_{P1}^k \tag{20a}$$

$$\phi_h = \sum_{k=1}^{N_n} N_i^k \hat{\phi}^k \tag{20b}$$

where N_i^k are the same basis functions used in the finite element model in “Appendix A”.

The resulting finite element system is solved. In the smoothing step, a nodal interpolation step is done in order to find the field values at the new nodes. Then, another interpolation is done to find the field value at a single integration point at the barycentre of the element.

3.3 Summary

A summary of the developed method is presented in algorithm 1.

Result: $\vec{v}_{t=0:T}, P_{t=0:T}, d_{t=0:T}$

1. Initialize \vec{v}_t, P_t and d_t ;
- for** $t = 0 : T$ **do**
 - $i \leftarrow 0, \vec{v}_i \leftarrow \vec{v}_t, P_i \leftarrow P_t$;
 - while** ($Res_1 > Tol_{NR}$ and $i < i_{max}$) **do**
 - Solve the system of Eqs. 27a, 27b and 27c using a Newton Raphson solver to obtain v_{i+1}, p_{i+1} ;
 - Compute the new plastic strain increment using Eqs. 9, 11 and 13;
 - $i \leftarrow i + 1$
 - end**
 - $v_t \leftarrow v_i$;
 - $p_t \leftarrow p_i$;
3. Compute $\mathcal{H}(\underline{x}, t)$ based on the new elastic and plastic strains using Eq. 5b;
4. Solve Eq. 27d with $\mathcal{H}(\underline{x}, t)$ to obtain $d_{t+\Delta t}$;
5. Check if the phase field value at each node exceeded the threshold;
6. compute new element size;
7. Check the volume quality for each element in the mesh.;
- if** ($Minimum\ mesh\ quality < Mesh\ quality\ threshold$) **then**
 - 8. Trigger remeshing and transport the mechanical fields;
- else**
 - Go to step 2;
- end**

end

4 Numerical results and validation

4.1 Symmetrically notched tension test

In this section, numerical validation of the implementation of Borden et al. [11] is done. The validation step is carried out with a fixed mesh. Figure. 4 shows the geometry and boundary conditions of a symmetrically notched tension test. A sensor is also placed at the middle of the distance between the two notches to trace the evolution of the phase field variable at different deformation levels. The material parameters used are: $E = 68.8$ GPa, $\nu = 0.33$, $\rho = 2700$ kg/m³,

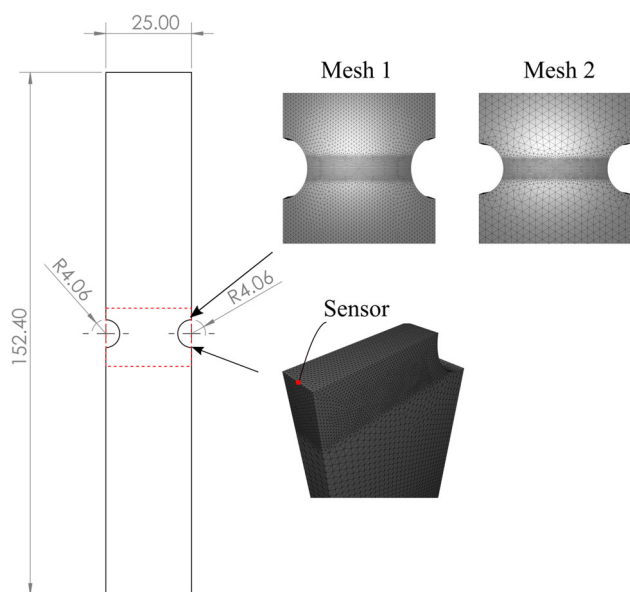


Fig. 4 The representation of the tension test geometry and boundary conditions of a reference case [11]. The mesh is illustrated with the local refinement. The thickness of the specimen is 2.37 mm where all dimensions are in mm

$\sigma_y = 320$ MPa, $H = 688$ MPa. The model parameters are: $\beta_1 = \beta_2 = 1$, $l_c = 0.6452$ mm $G_c = 60$ kJ/m² and $\zeta = 10^{-3}$.

In order to choose a suitable time step for performing the calculations, a convergence study is done with a plastic energy threshold $W_0 = 10$ MPa and results are illustrated in Fig. 5. Normalized stress refers to the applied force divided by the initial area of the narrowest cross section and normalized strain is the total displacement divided by the initial length of the specimen. From the results shown in Fig. 5, a time step of 0.05 sec is used for all subsequent simulations since it provides a good compromise between quality of results and CPU time. At the same time, one can observe that in the linear regime, the Normalized stress vs. Normalized strain curves are almost identical to the reference solution and hence a larger time step can be used without losing the solution accuracy.

Figure 6 shows a comparison with the implementation of [11] of the normalized stress vs. normalized strain curves for two different values of the plastic threshold W_0 . The curves are very close to the reference solution especially for $W_0 = 10$ MPa. It can be observed that there is a small shift between the curves of the current work and reference solution. This is most likely related to the type of spatial discretization used for the numerical simulations which is different than the one used in [11]. For the reference case, the computations were performed using a quadratic NURBS isogeometric spatial discretization [44] whereas in the present work a tetrahedral element is used. Figure 7 also shows the crack evolution for different values of the plastic threshold.

One can clearly observe that the phase field profile at the initiation phase depends on the threshold and hence it should be well calibrated in order to accurately track the crack evolution.

4.2 Double-edge symmetric tension test with remeshing

In this example, we show the numerical results of the phase field model obtained with the developed isotropic remeshing strategy. When remeshing is used, a constant mesh size is used in the whole initial domain. Then, a mesh refinement process is carried out in order to have a small enough element size in the regions in which the crack is expected to propagate. Two different base element sizes are compared for the values 0.5 mm and 1.25 mm. The numerical computations are carried out with two different base mesh sizes in order to illustrate the accuracy of the two field transfer operators. Results are compared with a reference case of an initial fixed mesh with local refinement as shown in Fig. 4. The same geometry and material properties as in Sect. 4.1 with a plastic work threshold equals to 10 MPa are used in all the simulations. Two fixed size meshes, mesh 1 and mesh 2, are used to compare the results with the cases where remeshing is adopted 4. Mesh 1 and mesh 2 have sizes of 0.5 mm and 1.25 mm in the domain, respectively. A minimum mesh size of 0.1613 mm is used in the region where the crack is expected to propagate. The specimen is fixed from the bottom and displaced from the upper end with a constant velocity of 0.0042 mm/sec. Two different thresholds of the phase field indicator function are used: 0.025 and 0.075.

Figure 8 shows the phase field evolution at four different strain states with the phase field threshold value equals to 0.025 and base mesh size set to 0.5 mm. The time step is set to 0.5 s for the first 125 increments since accurate results can be obtained in the linear regime with a large time step and then 0.05 s for the rest of the simulation since it is concluded from the time step convergence study that the proposed time step is a good compromise between accuracy and low computational time. The results are plotted on the current configuration where the mesh topology at the different states is shown. In Fig. 8a, the remeshing is not yet initiated since this is a very early deformation state, i.e., the same phase field distribution is obtained. Then, the remeshing operation is initiated with both transfer operators as shown in Fig. 8b.

The phase field profiles with a threshold value of 0.075 are shown in Fig. 9. Comparing Figs. 8c and 9c shows that when the phase field threshold is 0.075, the crack initiates and propagates at a larger displacement than the case of a threshold of 0.025. This can be explained by the fact that when the elements size in the damaged region are not sufficiently fine, the accuracy of the mechanical fields evolution is affected. In other words, when the remeshing initiation is

Fig. 5 Study of the time step convergence for the Normalized Stress vs. Normalized Strain curves. Time increments are in seconds

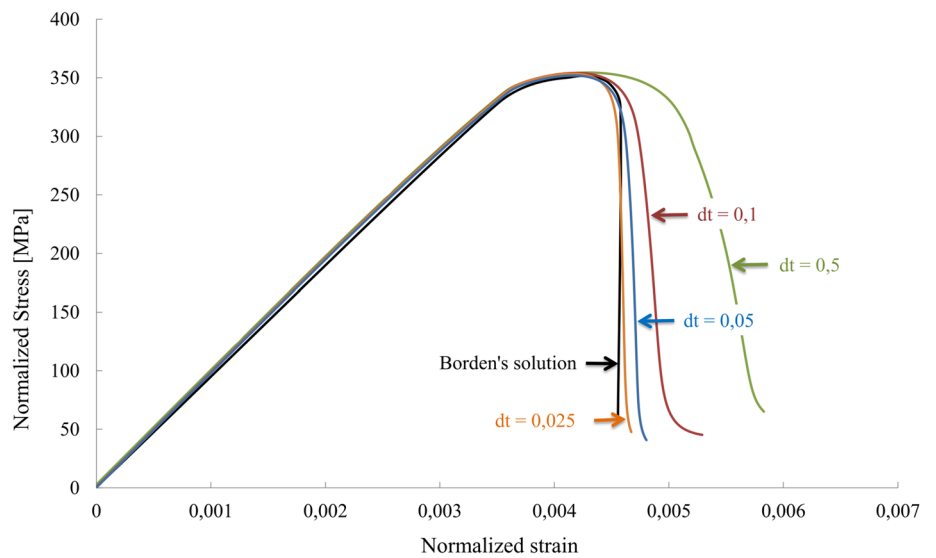


Fig. 6 Numerical validation with the model of M.J. Borden et al. [11]. Results are reported for two different values of the plastic threshold. The time step is set to 0.5 sec during the first 125 steps in the linear regime then 0.025 sec for the rest of the simulation

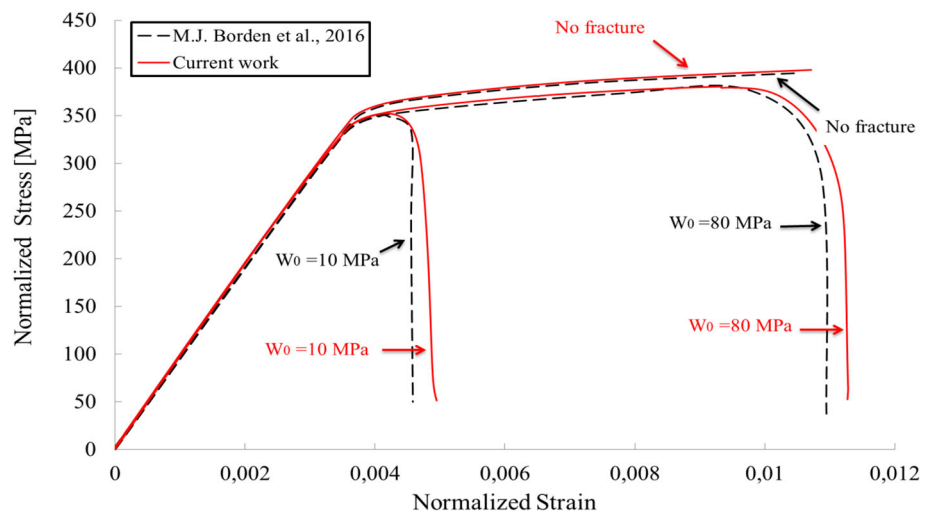


Fig. 7 Contour plots of the phase field evolution for three different values for the plastic threshold W_0 . Four different deformation states are illustrated starting from crack initiation at (a) until the final failure at (d)

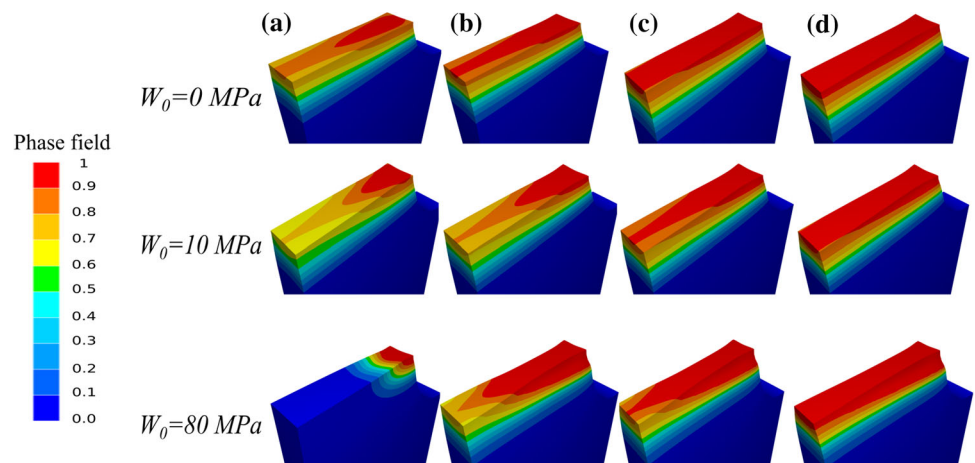


Fig. 8 Evolution of phase field at different deformation states on the deformed configuration for a phase field threshold is set to 0.025. **a** $u = 0.3028$ mm. The average element size of the base mesh is set to 0.5 mm. **b** $u = 0.3417$ mm. **c** $u = 0.3618$ mm. **d** $u = 0.3650$ mm

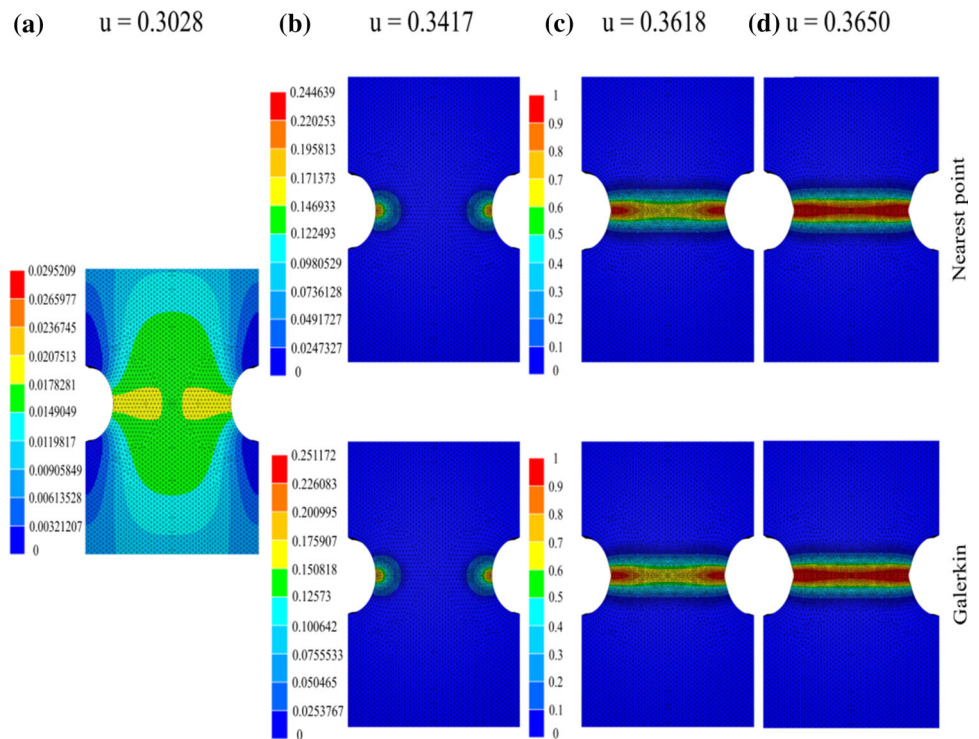
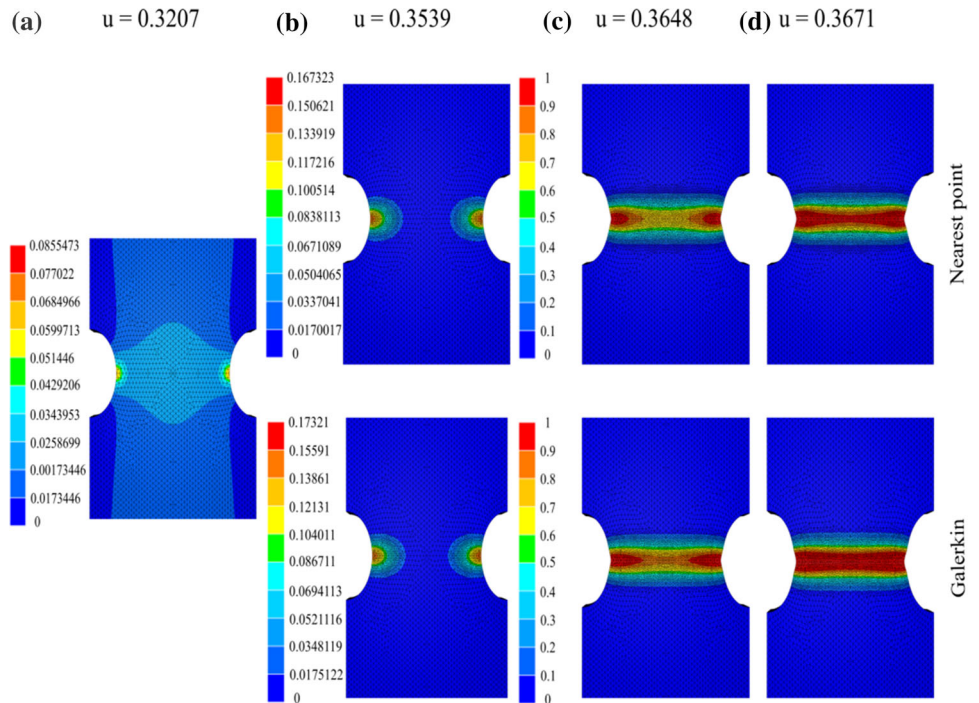


Fig. 9 Evolution of phase field at different deformation states on the deformed configuration for a phase field threshold is set to 0.075. The average element size of the base mesh is set to 0.5 mm. **a** $u = 0.3207$ mm. **b** $u = 0.3539$ mm. **c** $u = 0.3648$ mm. **d** $u = 0.3671$ mm



a lightly delayed, the exact moment of crack initiation is not accurately captured. In consequence, the full crack is formed at a displacement $u = 0.3671$ mm which is also higher than the case when the threshold is 0.025 as it is reported as $u = 0.3650$ mm.

It can also be observed in Fig. 9c that the crack propagates for a longer distance toward the center at the same

displacement when the Galerkin smoothing method is used. The reason for that is also related to the field transfer operation that affects the accuracy of the transported fields.

Figure 10 shows the Normalized Stress vs. Normalized Strain curves for different threshold values. Results are obtained for both field transfer operators and compared with the case of an initial fixed mesh. When the value of the thresh-

Fig. 10 Symmetrically notched specimen tension test. **a** Normalized Stress vs. Normalized Strain curves for two different values for the phase field threshold. A comparison is shown for the two field transfer operators with the reference case with an initial fixed mesh. The base element size = 0.5 mm

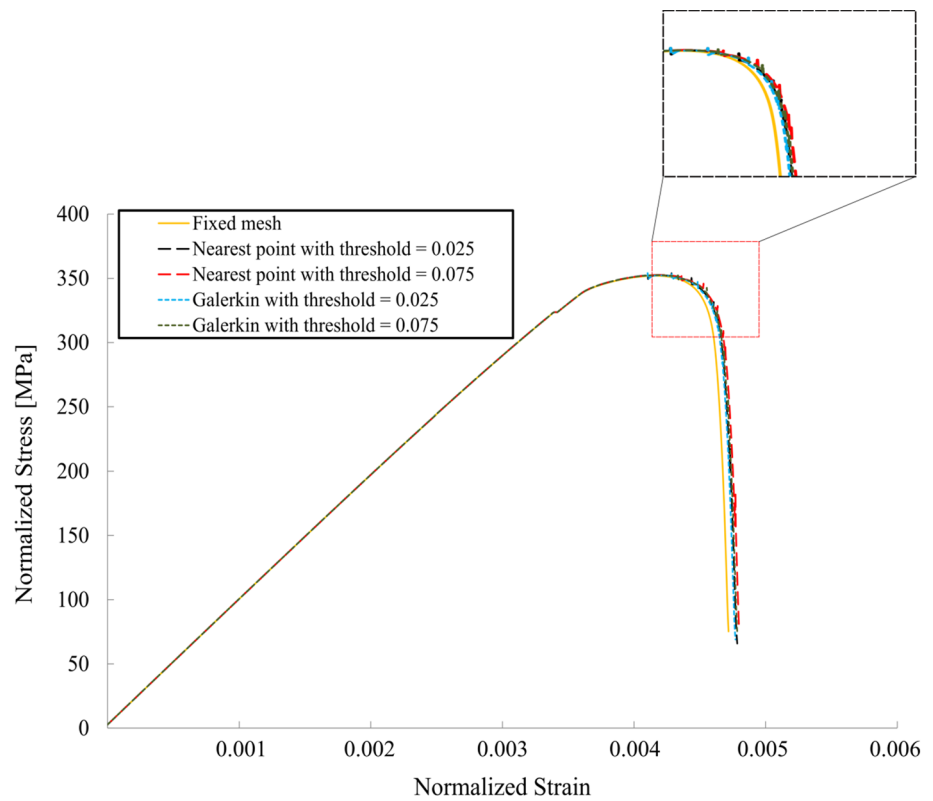


Table 1 Symmetrically notched tension test with base element size = 0.5 mm

Transfer operator	Threshold	Remeshing operations	Initial number of elements	Final number of elements	CPU run time [hour]
Fixed mesh			112080	112080	1.09
Galerkin smoothing	0.025	6	82477	125550	0.85
Galerkin smoothing	0.075	6	82477	111800	0.79
Nearest point	0.025	7	82477	130800	0.77
Nearest point	0.075	6	82477	117780	0.71

old is increased to 0.075, the coarse mesh topology before the initiation of the remeshing operations does not permit to capture the localized plastic strains at an early stage of the deformation and hence the crack initiation is delayed. Locally, Fig. 14a shows the local phase field evolution at a node shown in Fig. 4. It can be clearly observed that there is a small difference in the phase field profile between the remeshing and the reference cases.

The number of elements and run time² are reported in Table 1. It can be clearly observed that the number of elements in the end of simulations is even lower than the reference case since it is difficult to know where exactly the refinement should take place so we tend to enlarge the region of the refined mesh.

² The calculations are carried out using 6 processors on a workstation with an Intel® core™ i7-8700 CPU @ 3.2 GHz and a 32 GB RAM.

To conclude, the developed adaptive remeshing strategy results in a very accurate prediction of the crack initiation and propagation with a significant reduction in the computation time. It should be noted that the reduction factor in the element size from the beginning to the end of the computations was about 3 times. The next step is to test the model validity with a higher reduction ratio. A base element of size 1.25 mm is used with a reduction ratio to the final element size of about 7.75. Figures 11 and 12 show the phase field evolution profiles for two threshold values of 0.025 and 0.075, respectively.

In a general sense, for both threshold values the crack is initiated at a larger displacement than the cases with a base element size 0.5 mm. It can be observed again that displacements starting at the crack initiation until the complete failure are higher when the threshold 0.075 is used.

The same conclusion is drawn regarding the two field transfer operators; the crack propagates for a longer dis-

Fig. 11 Evolution of phase field at different deformation states on the deformed configuration for a phase field threshold is set to 0.025. The average element size of the base mesh is set to 1.25 mm. **a** $u = 0.3027$ mm. **b** $u = 0.3539$ mm. **c** $u = 0.3749$ mm. **d** $u = 0.3788$ mm

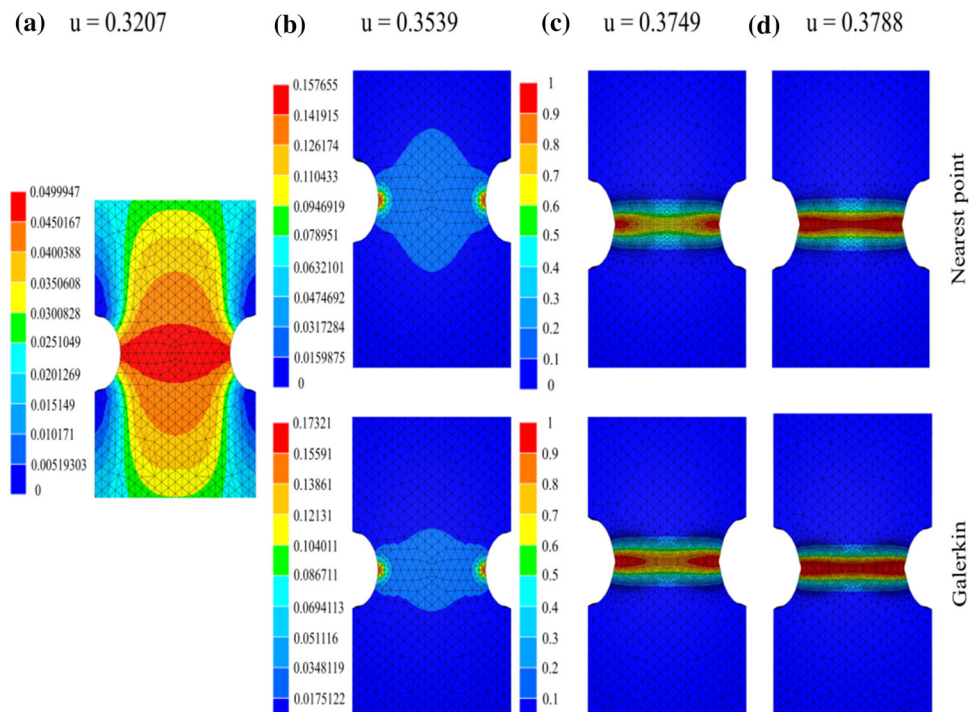
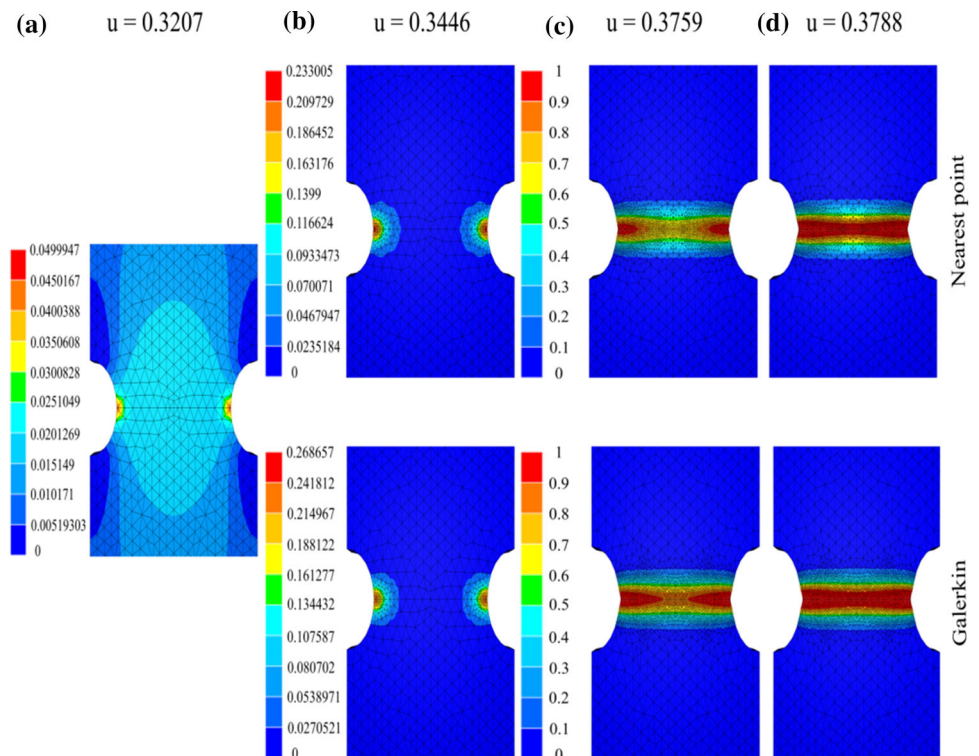


Fig. 12 Evolution of phase field at different deformation states on the deformed configuration for a phase field threshold is set to 0.075. The average element size of the base mesh is set to 1.25 mm. **a**. $u = 0.3207$ mm. **b**. $u = 0.3446$ mm. **c**. $u = 0.3759$ mm. **d**. $u = 0.3788$ mm



tance at the same displacement when the Galerkin smoothing method is used as shown in Figs. 11c and 12c.

The Normalized Stress vs. Normalized Strain curves are shown in Fig. 13. From a global view, there is a shift between the curves of fixed mesh and remeshing cases as compared to the case with a base element size of 0.5 mm. It

can be also observed that when a threshold of a value 0.025 is used, closer results to the reference solution are obtained. The behavior of the global response can be explained by the local evolution of the phase field as shown in Fig. 14b.

The initial and final number of elements along with the CPU run time are reported in Table 2. It can be clearly seen

Fig. 13 Normalized Stress vs. Normalized Strain curves for two different values for the phase field threshold. Comparison between the two field transfer operators with the reference case with an initial fixed mesh. The base element size = 1.25 mm

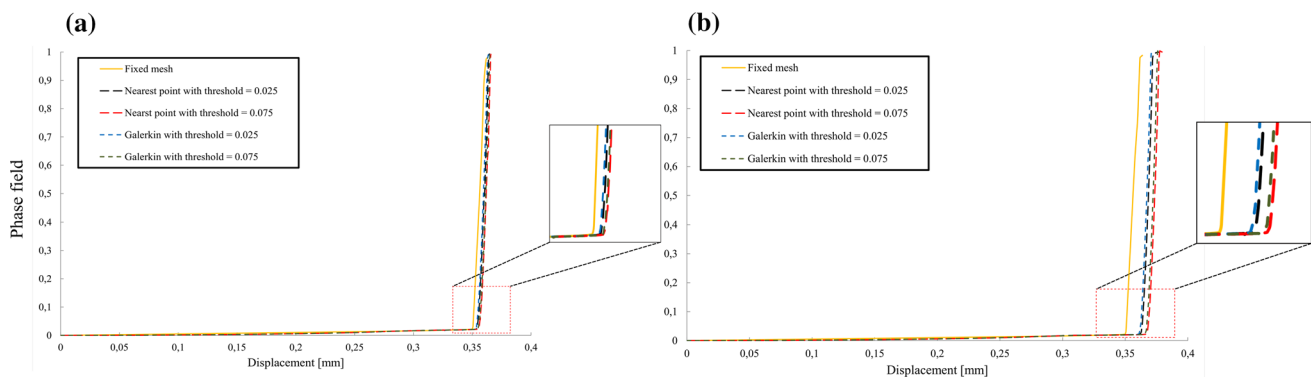
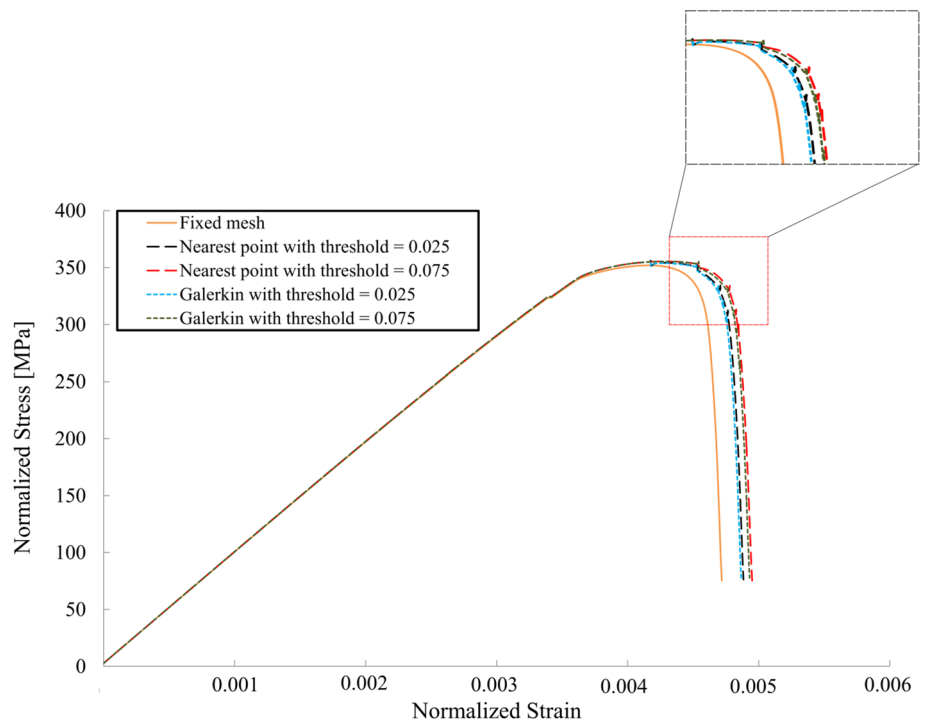


Fig. 14 Comparison between the phase field evolution at a fixed mesh and with remeshing with a base element size = 0.5 mm in **a** and 1.25 mm in **b**

Table 2 Symmetrically notched tension test with base element size = 1.25 mm

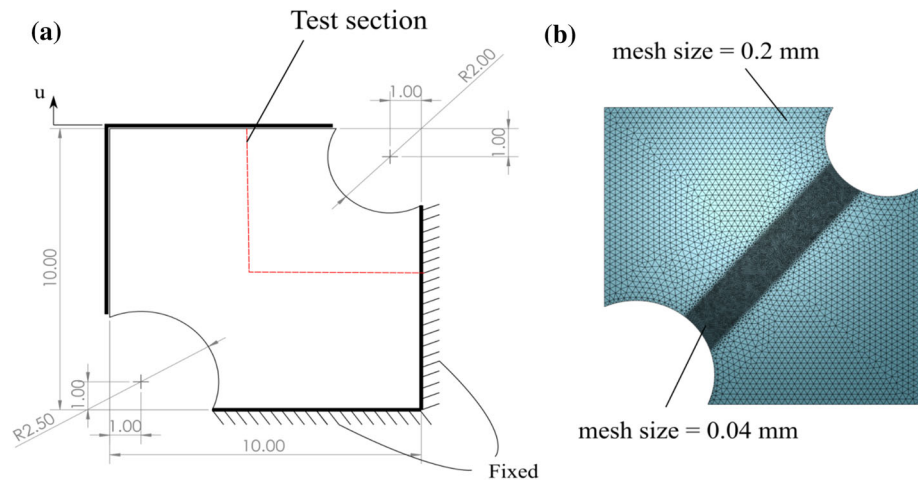
Transfer operator	Threshold	Remeshing operations	Initial number of elements	Final number of elements	CPU run time [hour]
Fixed mesh			52278	52278	0.57
Galerkin smoothing	0.025	7	7023	43688	0.15
Galerkin smoothing	0.075	5	7023	34618	0.14
Nearest point	0.025	4	7023	38326	0.15
Nearest point	0.075	4	7023	26119	0.11

that the initial and final number of elements are less than the case with a base element size of 0.5 mm, i.e., the computational time has drastically been reduced by a factor of nearly 4 in average.

The conclusion here is that, it is possible to get a significant decrease of computational time by using remeshing. How-

ever, the solution accuracy with remeshing is reduced when the initial element size is increased. In addition, the results are improved when the phase field threshold is reduced since the localization of plastic strain is well captured with the small element size, but the computational time is increased. In consequence, the developed computational framework can

Fig. 15 **a** Geometry and boundary conditions of a double notched specimen. **b** The mesh size of the reference case without remeshing. The thickness of the specimen is 0.2 mm. All dimensions are in mm



be adopted to have a good compromise between solution accuracy and computational time. Regarding the field transfer operators, the results show that the data diffusion is very similar for the two cases with a slight improvement exists when the Galerkin smoothing method is used. In the following example, the Galerkin smoothing method is adopted for all cases.

4.3 Double notched specimen

In this example, a double notched thin specimen is used to prove the ability of the developed algorithm to deal with complex crack paths efficiently. The geometry and boundary conditions of the specimen are shown in Fig. 15 [17] along with the mesh size distribution. The thickness of the specimen is chosen to be 0.2 mm. A quasi static loading is assumed, i.e., inertial effects are neglected. The material parameters are: $E = 180$ GPa, $\nu = 0.28$, $\sigma_y = 443$ MPa, $H = 300$ MPa.

The model parameters are: $W_0 = 80$ MPa, $\beta_1 = \beta_2 = 1$, $l_c = 0.04$ mm, $G_c = 20$ kJ/m² and $\zeta = 10^{-3}$. The Galerkin smoothing method is used for all simulations in this section.

Figure 16 shows the phase field evolution for a base element size of 0.2 mm where the phase field threshold is chosen to be 0.06. It should be noted that the choice of the numerical parameter η is tailored manually in all the following examples in order to obtain a similar number of remeshing operations i.e., the effect of data diffusion due to remeshing is eliminated. The loading velocity is set to 0.05 mm/sec. The time step is set to 0.01 sec in the first 200 steps since the level of the damage is still low and 0.002 for the rest of simulations in order to properly track the crack evolution.

The obtained phase field profile for this case indicates that the crack is initiated at the two notches which is the same observation as the reference case with a fixed mesh (this is the case which we consider as the most accurate). Then, the two crack branches propagate toward the center until merging

and leading to the final failure. It can also be observed that the evolution of the refined zone in the mesh follows the phase field evolution starting from the crack initiation until the complete failure.

Figure 17 shows the crack and mesh topology evolution with a base element size of 0.15 mm. The obtained cracking sequence is very similar to the case of a 0.2 mm mesh presented earlier. However, the specimen is completely fractured at a lower displacement as compared to the case of a 0.2 mm mesh size.

Figure 18 shows the phase field and mesh topology evolution with a remeshing indicator function that is based on the equivalent plastic strain with a threshold value equals to 0.06. The initial element size is 0.2 mm. Remeshing is initiated at an early stage in which the zone where the crack is expected to propagate is fully remeshed before the crack initiation, i.e., the maximum value of the phase field is not yet equal to 1. It can be also observed that the refined zone is wider than the cases where the phase field is used as an indicator function. This observation is confirmed with the final number of elements in this case which is reported in Table 3 as compared to the case where a phase field remeshing indicator function is used with the same initial element size.

Figure 19 shows the evolution of the equivalent plastic strain at two different displacements where three remeshing indicator functions are used: phase field, equivalent plastic strain and normalized yielding functions. It can be observed that the error of the equivalent plastic strain with respect to the reference case is reduced when a plastic strain threshold is used. This can be related to the fact that when the mesh size is reduced earlier, more accurate calculation of the equivalent plastic strain is obtained since the strain localization is properly captured; hence the phase field evolution becomes more accurate.

Fig. 16 Phase field evolution at various deformation stages on the deformed configuration for a fine mesh with base element size 0.2 mm. The phase field is used to trigger the remeshing with a threshold of 0.06. The mesh topology is shown at each stage. **a** $u = 0.2698$ mm. **b** $u = 0.2796$ mm. **c** $u = 0.3535$ mm

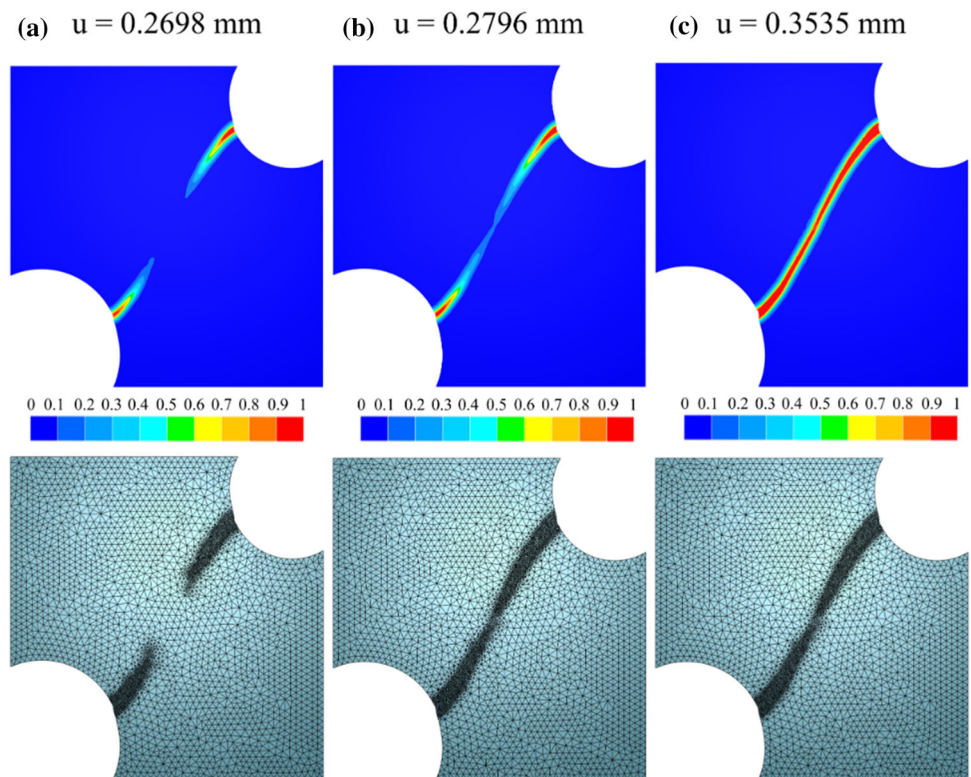


Fig. 17 Phase field evolution at various deformation stages on the deformed configuration with base element size 0.15 mm. The phase field is used to trigger the remeshing with a threshold of 0.06. The mesh topology is shown at each stage. **a** $u = 0.2297$ mm. **b** $u = 0.2547$ mm. **c** $u = 0.3180$ mm

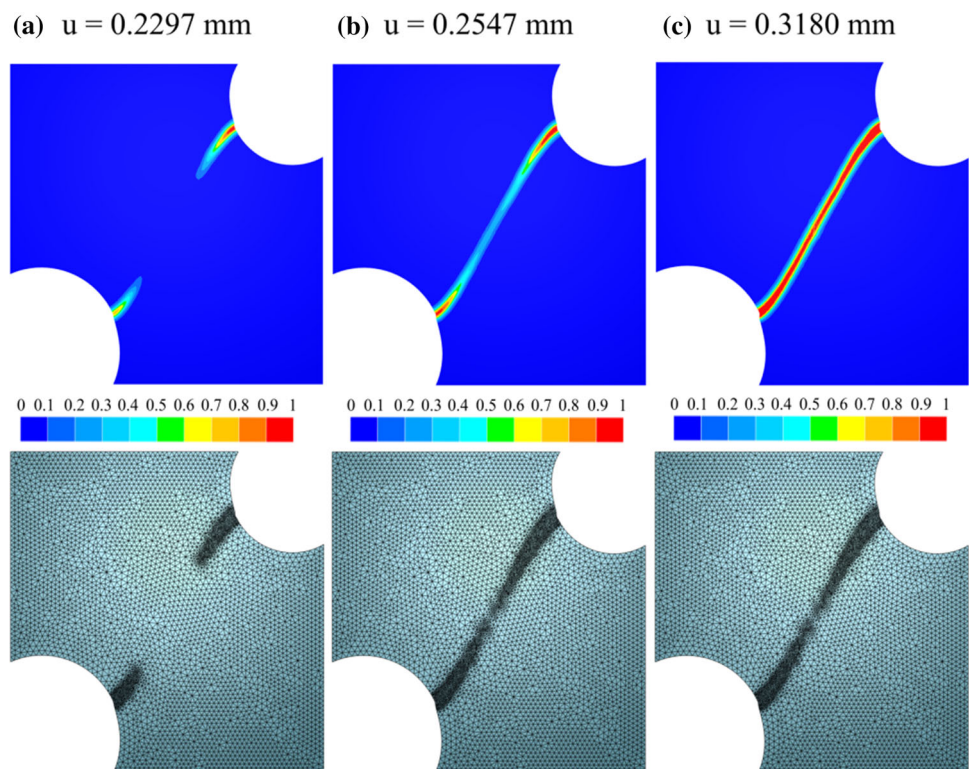


Fig. 18 Phase field evolution at various deformation stages on the deformed configuration with base element size 0.2 mm. The equivalent plastic strain is used to trigger the remeshing with a threshold of 0.06. The mesh topology is shown at each stage. **a** $u = 0.2249$ mm. **b** $u = 0.2421$ mm. **c** $u = 0.2592$ mm

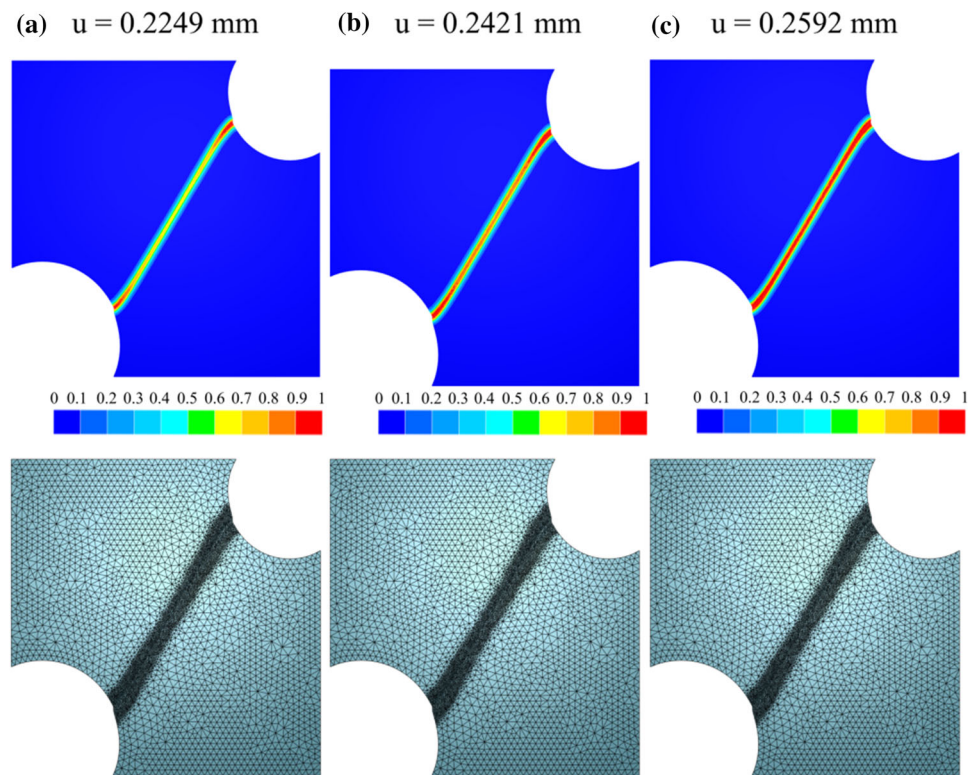


Table 3 Double notched specimen performance analysis

Threshold	η	Threshold value	Base element size [mm]	Initial nb. of elements	Final nb. of elements	CPU time [hour]	Energy error %
Fixed mesh				182900	182900	2.25	
PF	1	0.06	0.15	23663	48193	0.8	50.7
PF	0.8	0.06	0.2	13046	41904	0.7	54.86
EQP	0.8	0.06	0.2	13046	70677	1.05	20
EQP	0.8	0.001	0.2	13046	148300	1.97	4.9
NYF	1.25	0.0001	0.2	13046	36113	0.93	2.7

The normalized yielding function NYF defined in Eq. 21 is used as another remeshing indicator function.

$$NYF = \frac{f^{trial}}{\sigma_{VM}(\mathbf{u}, d)} \quad (21)$$

with this indicator function, the number of elements is reduced over time since the stress far from the crack lips (damaged region) is degraded due to the creation of the crack surface as shown in Fig. 20.

The Force vs. Displacement curves are shown in Fig. 21 and. Comparing the results when remeshing is used for two mesh sizes with the reference case shows that the initial element size plays an important role in determining the moment at which the softening phase begins. Furthermore, when the mesh adaptation is based on the phase field variable, the element size in the region of interest will be only modified when the plastic energy exceeds the threshold W_0 , i.e., the phase

field evolution is mainly governed by the plastic strains. The values of plastic strain will not be close enough to the reference case as to accurately contribute to the phase field evolution, hence the crack initiation is delayed. So, it seems convenient in such case to adapt the mesh based on the plastic strain or yielding function rather than the phase field variable so that the evolution of plastic strains becomes more conservative.

Table 3 shows the performance analysis for different cases along with the fixed mesh case. It can be seen that a reduction of the equivalent plastic strain threshold to 0.001 leads to results very close to the reference case with a fixed mesh at a computational cost reduced by a about 12%. In addition, when the normalized yielding function is used, the computational time is reduced by a factor of 59 % while the results are very close to the reference case with a fixed mesh. In addition, an energy error is found in the same table for each

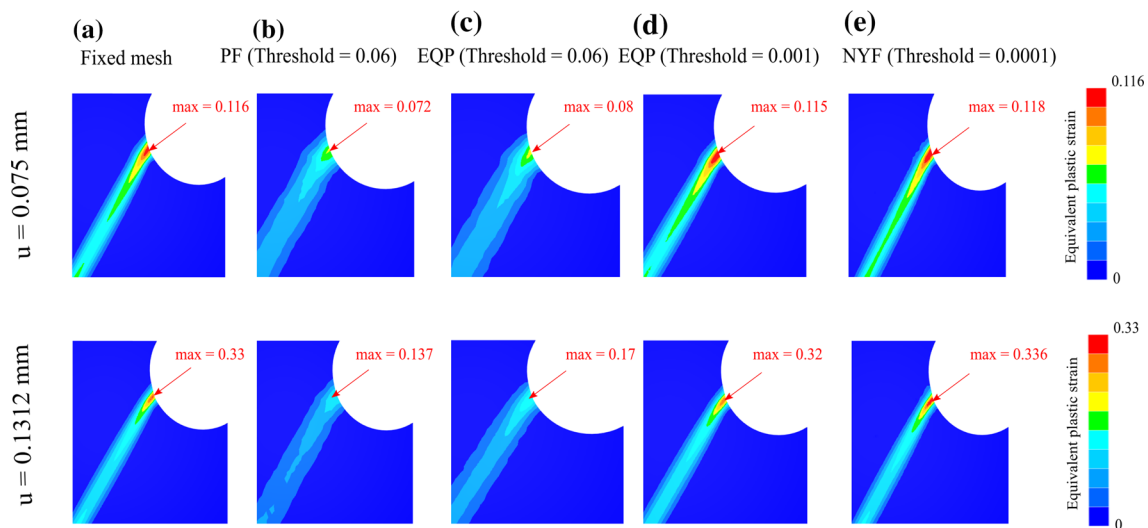
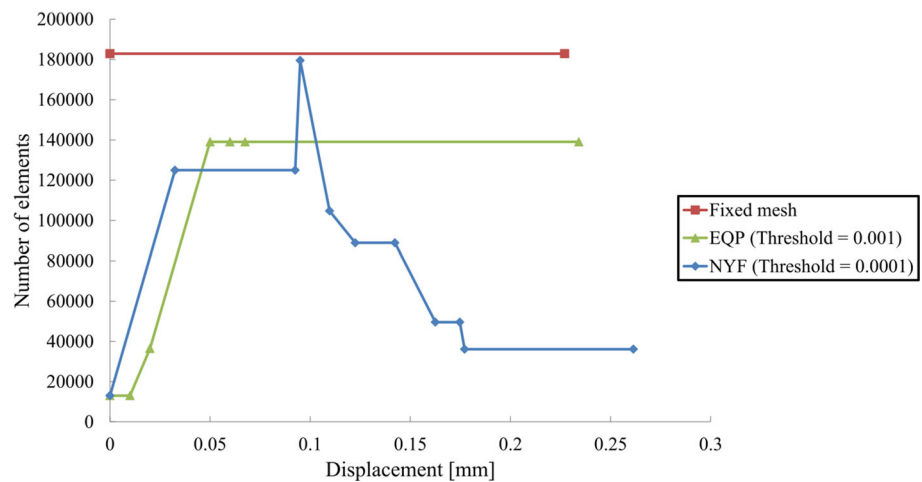


Fig. 19 Evolution of equivalent plastic strain at two different displacements. Comparison is carried out between the reference case with no remeshing, remeshing with phase field (PF) threshold, two equivalent plastic strain thresholds (EQP) and normalized yielding function (NYF)

Fig. 20 Evolution of number of elements for different remeshing cases along with the reference case (Fixed mesh)



threshold type. The energy error is calculated as follows

$$\text{Energy error } \% = \frac{\int_0^{r_{max}} (F_{remesh} - F_{ref}) dr}{\int_0^{r_{max}} F_{ref} dr} \quad (22)$$

where F_{remesh} is the force obtained with remeshing, F_{ref} is the force obtained from the reference case with a fixed mesh, r is the displacement and r_{max} is the maximum displacement. The energy error helps in quantifying the energy loss for each method. It can be seen that the normalized yielding function gives the lowest possible energy loss among the others which proves its accuracy.

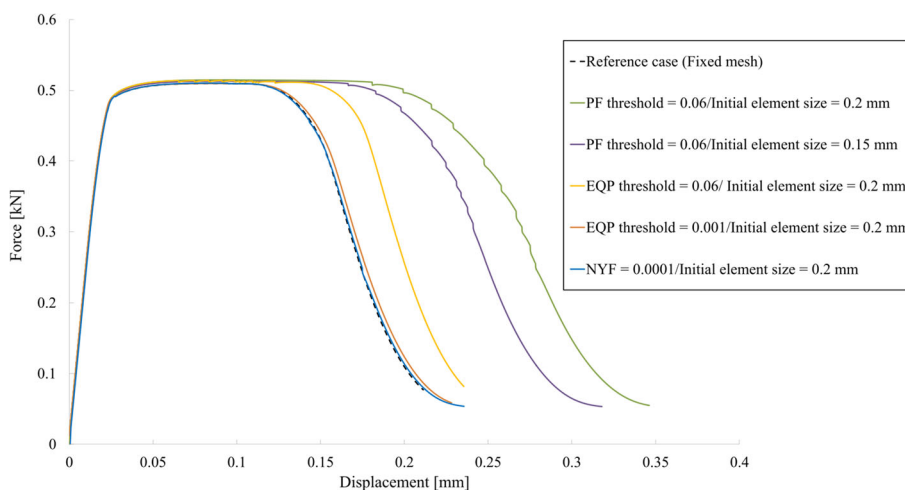
To conclude, the proposed adaptive remeshing strategy provides a flexible compromise between accuracy and computational cost. Depending on the application, whether the phase field or the equivalent plastic strain can be used to trigger remeshing. When the normalized yielding function is used, the obtained results are very close to the reference case

with a significant reduction in the computation time; hence this criterion seems to be the most suitable to be used.

5 Conclusion and perspectives

The main advantage of the phase field model is the ability to model fracture processes without any special treatment for the crack initiation and propagation. In order to enhance the efficiency of the computational model, an adaptive isotropic remeshing strategy is coupled with a phase field model of ductile fracture. The proposed strategy offers a robust tool for predicting initiation and propagation of complex crack path in highly ductile materials. This paper analysed both qualitatively and quantitatively two applications with different levels of complexity: a straight crack path between two notches having the same sizes and a diagonal crack formed in a non symmetric notched specimen.

Fig. 21 Force vs. Displacement curves for different remeshing cases along with the reference case (Fixed mesh). *NYF* is the normalized trial yield function



Two different field transfer operators are used in order to efficiently remap the mechanical fields: (i). the nearest point interpolation; (ii). the Galerkin smoothing method. The former is considered as the simplest approach since a direct interpolation is done for each integration point, however its accuracy is dependent on the size of mesh and the gradient of remapped field. While the latter is more computationally expensive since a smoothing step is needed to transform the P_0 field to a P_1 field. The results presented in this paper show some differences using both mapping techniques. However, a lower amount of data diffusion is usually obtained using the Galerkin smoothing method.

In order to minimize the data loss in the transfer process, two different thresholds were used: (i). a remeshing indicator function threshold that is used to locate the regions where the mesh should be refined; (ii). a volume quality threshold that controls the number of remeshing operations so that the data loss is minimized and the numerical strategy becomes more conservative.

A comparison is carried out between the results when a phase field, equivalent plastic strain and normalized yielding stress indicator functions are used. Results have shown that in some cases where the contribution of the plastic strain in the phase field evolution is delayed, the mesh in the damaged region will be refined lately; hence the evolution of the plastic strain will not be accurate. On the other hand, when both the equivalent plastic strain and normalized yielding functions are used to trigger the remeshing, the mesh will be refined at an early stage, so the evolution of the plastic strain will be conservative for an accurate prediction for the crack initiation and propagation. Unfortunately, when the equivalent plastic strain is used, the remeshed region becomes wider with higher number of elements; hence the computation time is increased as shown in the performance tables for all the examples. On the other hand, when the normalized yielding function is used, the final number of elements is decreased

due to the localization of plastic strains around the damaged region. The recorded CPU times vary with each threshold depending on the threshold type and value, but it can be seen that the normalized yielding function gives the best possible precision with respect to the reference case with a fixed mesh with the lowest computational time.

Several extensions are possible in the future to the developed framework. For example, testing the ability of the model to predict complex fracture modes in metal forming applications for which crack paths are not known a priori. In such applications, the plastic strains are very large and special treatment of the crack driving force is needed to include the effect of stress triaxiality. An adaptive time scheme would also be interesting in order to obtain the most efficient solution from the computational point of view when combined with mesh adaptivity.

A Weak formulation of the problem

In this section, the weak form of the phase field for ductile fracture and mechanical equations is demonstrated within the framework of mixed velocity/pressure formulation. The strong form of mechanical equations is written as

$$\rho \frac{\partial \vec{v}}{\partial t} = \vec{\nabla} \cdot \vec{s} - \vec{\nabla} p + \rho \vec{g} \quad (\text{Conservation of linear momentum}) \tag{23a}$$

$$\vec{\nabla} \cdot \vec{v} = -\frac{\dot{p}}{\kappa} \quad (\text{Conservation of mass}) \tag{23b}$$

$$\vec{v} = \vec{v}_0 \text{ on } \partial\Omega_v \quad (\text{Dirichlet boundary condition}) \tag{23c}$$

$$\vec{t} = \vec{t}_0 \text{ on } \partial\Omega_t \quad (\text{Neumann boundary condition}) \tag{23d}$$

$$\partial\Omega_h = \partial\Omega_v \cup \partial\Omega_t$$

where s is the deviatoric part of the Cauchy stress tensor, p is the pressure, \vec{v} is the velocity vector, κ is the bulk’s modulus, ρ is the material density and \vec{g} is the body force vector per unit mass. The boundary conditions are illustrated in Fig. 1. Ω_h is the solid domain in the current configuration, $\partial\Omega_v$ and $\partial\Omega_t$ are the predefined boundaries for Dirichlet and Neumann boundary conditions, respectively. The finite element method is used to solve the system of Eqs. 5 and 23. Following the standard Galerkin formulation by multiplying the strong form of partial differential equations by the appropriate test functions leads to the weak form of the following problem: Find $(\vec{v}_h, p_h$ and $d_h) \in \mathcal{V}_h \otimes \mathcal{P}_h \otimes \mathcal{D}_h$

$$\int_{\Omega_h} \left(\rho \frac{\partial \vec{v}_h}{\partial t} \cdot \vec{v}_h^* + s(\vec{v}_h) : \dot{\epsilon}(\vec{v}_h^*) - p_h \vec{\nabla} \cdot \vec{v}_h^* - \rho \vec{g} \cdot \vec{v}_h^* \right) d\Omega_h = \int_{\partial\Omega_t} \vec{t}_0 \cdot \vec{v}_h^* d\partial\Omega_h \tag{24a}$$

$$\int_{\Omega_h} p_h^* \vec{\nabla} \cdot \vec{v}_h + \frac{p_h^* \dot{p}_h}{\kappa} d\Omega_h = 0 \tag{24b}$$

$$\int_{\Omega_h} \frac{G_c}{l_c} d_h^* d_h + \int_{\Omega_h} G_c l_c \nabla d_h^* \cdot \nabla d_h d\Omega_h - \int_{\Omega_h} d_h^* \mathcal{H} d\Omega_h = 0 \tag{24c}$$

$$\forall \vec{v}_h^*, p_h^*, d_h^* \in \mathcal{V}_h^0 \otimes \mathcal{P}_h^0 \otimes \mathcal{D}_h^0 \tag{24d}$$

$$\mathcal{V}_h = \left\{ v_h \in (H^1)^{\dim(\Omega_h)}, \vec{v}_h = \vec{v}_0 \text{ on } \partial\Omega_e, \forall e \in N_e \right\}$$

$$\mathcal{P}_h = \left\{ p_h \in (C^0)^{\dim(\Omega_e)} \cap L^2, p_h \in P^1 \text{ in } \Omega_e, p_h = p_0 \text{ on } \partial\Omega_e, \forall e \in N_e \right\}$$

$$\mathcal{D}_h = \left\{ d_h^* \in (C^0)^{\dim(\Omega_h)} \cap H^1, d_h \in P^1 \text{ in } \Omega_e, d_h = d_0 \text{ on } \partial\Omega_e, \forall e \in N_e \right\}$$

$$\mathcal{V}_h^0 = \left\{ v_h^* \in \mathcal{V}_h^0, \vec{v}_h = 0 \text{ on } \partial\Omega_e, \forall e \in N_e \right\}$$

$$\mathcal{P}_h^0 = \left\{ p_h^* \in \mathcal{P}_h^0, p_h = 0 \text{ on } \partial\Omega_e, \forall e \in N_e \right\}$$

$$\mathcal{D}_h^0 = \left\{ d_h^* \in \mathcal{D}_h^0, d_h = 0 \text{ on } \partial\Omega_e, \forall e \in N_e \right\}$$

the test functions are chosen to be the variations of the unknown variables so that the kinematic admissibility conditions are satisfied at the boundaries. Ω_h is the volume of a finite element mesh at the current configuration so that

$$\Omega_h = \bigcup_e \Omega_e \quad (e \in N_e)$$

where N_e is the number of elements in the mesh.

A.1 Finite element model

In order to ensure the well-posedness and stability of the numerical solution, a bubble function is introduced to enrich the velocity field. The bubble function should have a value of 1 at the center of the element and vanishes at the boundaries, the resulting velocity and pressure fields of an element in the mesh can be expressed as

$$\vec{v}_h = \vec{v}_l + \vec{v}_b = \sum_{k=1}^{N_n} N_l^k \vec{v}_l^k + \sum_{j=1}^{N_e} N_b^k \vec{v}_b^k \tag{25a}$$

$$p_h = \sum_{k=1}^{N_n} N_l^k P^k \tag{25b}$$

$$d_h = \sum_{k=1}^{N_n} N_l^k d^k \tag{25c}$$

$$p_h = \sum_{k=1}^{N_n} N_l^k P^k$$

$$d_h = \sum_{k=1}^{N_n} N_l^k d^k$$

where N_l^k and N_b^k are the base and bubble interpolation functions associated with node k , respectively. N_e and N_n are the number of elements and nodes respectively. The resulting system of equations can be written as

$$\int_{\Omega_h} \rho \frac{\partial \vec{v}_l}{\partial t} \cdot \vec{v}_l^* + s(\vec{v}_l) : \dot{\epsilon}(\vec{v}_l^*) - p_h \vec{\nabla} \cdot \vec{v}_l^* - \rho \vec{g} \cdot \vec{v}_l^* d\Omega_h = \int_{\partial\Omega_t} \vec{t}_0 \cdot \vec{v}_l^* d\Omega_h \tag{26a}$$

$$\int_{\Omega_h} \rho \frac{\partial \vec{v}_b}{\partial t} \cdot \vec{v}_b^* + s(\vec{v}_b) : \dot{\epsilon}(\vec{v}_b) - p_h \vec{\nabla} \cdot \vec{v}_b d\Omega_h = \int_{\Omega_h} \rho \vec{g} \cdot \vec{v}_b^* d\Omega_h \tag{26b}$$

$$\int_{\Omega_h} p_h^* \vec{\nabla} \cdot (\vec{v}_l + \vec{v}_b) + \frac{p_h^* \dot{p}_h}{\kappa} d\Omega_h = 0 \tag{26c}$$

$$\int_{\Omega_h} \frac{G_c}{l_c} d_h^* d_h d\Omega_h + \int_{\Omega_h} G_c l_c \frac{\partial d_h}{\partial \vec{x}} \cdot \frac{\partial d_h^*}{\partial \vec{x}} d\Omega_h - \int_{\Omega_h} d_h^* \mathcal{H} d\Omega_h = 0 \tag{26d}$$

$$\mathcal{L}_l^0 = \left\{ \vec{v}_l^* \in (C^0)^{\dim(\Omega_e)} \cap \mathcal{V}_l^0, \vec{v}_l^* \in P^1 \text{ in } \Omega_e, \vec{v}_l^* = 0 \text{ on } \partial\Omega_e, \forall e \in N_e \right\}$$

$$\mathcal{L}_b^0 = \left\{ \vec{v}_b^* \in (C^0)^{\dim(\Omega_h)}, \vec{v}_b^* \in P^1 \text{ in } \Omega_e, \vec{v}_b^* = 0 \text{ on } \partial\Omega_e, \forall e \in N_e \right\}$$

with the following properties taken into account: $\int_{\partial\Omega_t} \vec{t}_0 \cdot \vec{v}_l^* d\Omega_h = 0$ since the bubble function vanishes at the boundaries, the inertial contribution of the bubble part is neglected so that $\int_{\Omega_h} \rho \frac{\partial \vec{v}_l}{\partial t} \cdot \vec{v}_b^* d\Omega_h = \int_{\Omega_h} \rho \frac{\partial \vec{v}_b}{\partial t} \cdot \vec{v}_l^* d\Omega_h = 0$ and $\int_{\Omega_h} \mathbf{s}(\vec{v}_b) : \dot{\mathbf{e}}(\vec{v}_l^*) d\Omega_h = \int_{\Omega_h} \mathbf{s}(\vec{v}_l) : \dot{\mathbf{e}}(\vec{v}_b^*) d\Omega_h = 0$ due to the orthogonality property of the bubble and nodal spaces. The time derivative of the velocity is approximated as follows

$$\frac{\partial \vec{v}_{l,b}}{\partial t} = \frac{\vec{v}_{l,b}^{t+\Delta t} - \vec{v}_{l,b}^t}{\Delta t}$$

where Δt is the time step. Substituting Eq. 25 in 26, the final form of the residual equations can be written on the following form:

$$\mathbf{R}^{ll} + \mathbf{R}^{lp} = \mathbf{0} \quad (27a)$$

$$\mathbf{R}^{bb} + \mathbf{R}^{bp} = \mathbf{0} \quad (27b)$$

$$\mathbf{R}^{pl} + \mathbf{R}^{pb} + \mathbf{R}^{pp} = \mathbf{0} \quad (27c)$$

$$\mathbf{R}^{dd} + \mathbf{R}^{dl} = \mathbf{0} \quad (27d)$$

where \mathbf{R}^{xy} is the residual force vector of coupled set of unknowns x and y . The system of equations in 27 will be solved in a staggered manner. A Newton Raphson nonlinear solver is used to solve the system of the first three equations before each remeshing step. Then, the fourth equation will be solved independently. It is worth noting that the system of Eqs. 27a, 27b and 27c are condensed so that the final unknowns become the velocities and pressures at the nodes without the need to explicitly solving for the bubble velocities.

References

1. Francfort GA, Marigo J-J (1998) Revisiting brittle fracture as an energy minimization problem. *J Mech Phys Solids* 46
2. Mumford D, Shah J (1989) Optimal approximations by piecewise smooth functions and associated variational problems. *Commun Pure Appl Math* 42:577–685
3. Ambrosio L, Tortorelli VM (1990) Approximation of functional depending on jumps by elliptic functional via t-convergence. *Commun Pure Appl Math* 43:999–1036
4. Bourdin B, Francfort GA, Marigo J-J (2000) Numerical experiments in revisited brittle fracture. *J Mech Phys Solids* 48:797–826
5. Hofacker M, Miehe C (2012) Continuum phase field modeling of dynamic fracture: variational principles and staggered fe implementation. *Int J Fract* 178:113–129
6. Miehe C, Hofacker M, Welschinger F (2010) A phase field model for rate-independent crack propagation: Robust algorithmic implementation based on operator splits. *Comput Methods Appl Mech Eng* 199:2765–2778
7. Heider Y, Markert B (2017) A phase-field modeling approach of hydraulic fracture in saturated porous media. *Mech Res Commun* 80:38–46
8. Ambati M, Gerasimov T, De Lorenzis L (2015) Phase-field modeling of ductile fracture. *Comput Mech* 55:1017–1040
9. Aldakheel F, Wriggers P, Miehe C (2018) A modified gurson-type plasticity model at finite strains: formulation, numerical analysis and phase-field coupling. *Comput Mech* 62:815–833
10. Ambati M, Kruse R, De Lorenzis L (2016) A phase-field model for ductile fracture at finite strains and its experimental verification. *Comput Mech* 57:149–167
11. Borden MJ, Hughes TJ, Landis CM, Anvari A, Lee IJ (2016) A phase-field formulation for fracture in ductile materials: Finite deformation balance law derivation, plastic degradation, and stress triaxiality effects. *Comput Methods Appl Mech Eng* 312:130–166
12. Miehe C, Hofacker M, Schänzel L-M, Aldakheel F (2015) Phase field modeling of fracture in multi-physics problems. Part II. coupled brittle-to-ductile failure criteria and crack propagation in thermo-elastic-plastic solids. *Comput Methods Appl Mech Eng* 294:486–522
13. Miehe C, Aldakheel F, Raina A (2016) Phase field modeling of ductile fracture at finite strains: a variational gradient-extended plasticity-damage theory. *Int J Plast* 84:1–32
14. Dittmann M, Aldakheel F, Schulte J, Schmidt F, Krüger M, Wriggers P, Hesch C (2020) Phase-field modeling of porous-ductile fracture in non-linear thermo-elasto-plastic solids. *Comput Methods Appl Mech Eng* 361:112730
15. Gurson A. L (1977) Continuum theory of ductile rupture by void nucleation and growth: Part i-yield criteria and flow rules for porous ductile media
16. Needleman A, Tvergaard V (1984) An analysis of ductile rupture in notched bars. *J Mech Phys Solids* 32:461–490
17. Ambati M, Gerasimov T, De Lorenzis L (2015) A review on phase-field models of brittle fracture and a new fast hybrid formulation. *Comput Mech* 55:383–405
18. Babuška I (1973) The finite element method with lagrangian multipliers. *Numer Math* 20:179–192
19. Pierre R (1995) Optimal selection of the bubble function in the stabilization of the p1–p1 element for the stokes problem. *SIAM J Numer Anal* 32:1210–1224
20. Patil R, Mishra B, Singh I (2018) An adaptive multiscale phase field method for brittle fracture. *Comput Methods Appl Mech Eng* 329:254–288
21. Nagaraja S, Elhaddad M, Ambati M, Kollmannsberger S, De Lorenzis L, Rank E (2019) Phase-field modeling of brittle fracture with multi-level hp-fem and the finite cell method. *Comput Mech* 63:1283–1300
22. Noii N, Aldakheel F, Wick T, Wriggers P (2020) An adaptive global-local approach for phase-field modeling of anisotropic brittle fracture. *Comput Methods Appl Mech Eng* 361:112744
23. Heister T, Wheeler MF, Wick T (2015) A primal-dual active set method and predictor-corrector mesh adaptivity for computing fracture propagation using a phase-field approach. *Comput Methods Appl Mech Eng* 290:466–495
24. Muixí A, Fernández-Méndez S, Rodríguez-Ferran A (2020) Adaptive refinement for phase-field models of brittle fracture based on nitsche's method. *Comput Mech*, pp. 1–17
25. Patil R, Mishra B, Singh I (2018) A local moving extended phase field method (lmxfm) for failure analysis of brittle materials. *Comput Methods Appl Mech Eng* 342:674–709
26. Zhou S, Zhuang X (2018) Adaptive phase field simulation of quasi-static crack propagation in rocks. *Underground Space* 3:190–205
27. Hussein A, Aldakheel F, Hudobivnik B, Wriggers P, Guidault P-A, Allix O (2019) A computational framework for brittle crack-propagation based on efficient virtual element method. *Finite Elem Anal Des* 159:15–32
28. Aldakheel F, Hudobivnik B, Hussein A, Wriggers P (2018) Phase-field modeling of brittle fracture using an efficient virtual element scheme. *Comput Methods Appl Mech Eng* 341:443–466

29. Aldakheel F, Hudobivnik B, Wriggers P (2019) Virtual element formulation for phase-field modeling of ductile fracture. *Int J Multiscale Comput Eng* 17
30. Hussein A, Hudobivnik B, Wriggers P (2020) A combined adaptive phase field and discrete cutting method for the prediction of crack paths. *Comput Methods Appl Mech Eng* 372:113329
31. Kumar S, Fourment L, Guerdoux S (2015) Parallel, second-order and consistent remeshing transfer operators for evolving meshes with superconvergence property on surface and volume. *Finite Elem Anal Des* 93:70–84
32. Miehe C, Welschinger F, Hofacker M (2010) Thermodynamically consistent phase-field models of fracture: variational principles and multi-field fe implementations. *Int J Numer Meth Eng* 83:1273–1311
33. Noell PJ, Carroll JD, Boyce BL (2018) The mechanisms of ductile rupture. *Acta Mater* 161:83–98
34. Hibbitt HD, Marcal PV, Rice JR (1970) A finite element formulation for problems of large strain and large displacement. *Int J Solids Struct* 6:1069–1086
35. Bathe K-J, Ramm E, Wilson EL (1975) Finite element formulations for large deformation dynamic analysis. *Int J Numer Meth Eng* 9:353–386
36. Amor H, Marigo J-J, Maurini C (2009) Regularized formulation of the variational brittle fracture with unilateral contact: Numerical experiments. *J Mech Phys Solids* 57:1209–1229
37. Lee N-S, Bathe K-J (1994) Error indicators and adaptive remeshing in large deformation finite element analysis. *Finite Elem Anal Des* 16:99–139
38. Perić D, Hochard C, Dutko M, Owen D (1996) Transfer operators for evolving meshes in small strain elasto-plasticity. *Comput Methods Appl Mech Eng* 137:331–344
39. Wiberg N-E, Abdulwahab F, Ziukas S (1995) Improved element stresses for node and element patches using superconvergent patch recovery. *Commun Numer Methods Eng* 11:619–627
40. Zienkiewicz OC, Zhu J (1992) The superconvergent patch recovery (spr) and adaptive finite element refinement. *Comput Methods Appl Mech Eng* 101:207–224
41. Mediavilla J, Peerlings R, Geers M (2006) A robust and consistent remeshing-transfer operator for ductile fracture simulations. *Comput Struct* 84:604–623
42. Boroomand B, Zienkiewicz O (1999) Recovery procedures in error estimation and adaptivity. Part II: Adaptivity in nonlinear problems of elasto-plasticity behaviour. *Comput Methods Appl Mech Eng* 176:127–146
43. Brancherie D, Villon P (2006) Diffuse approximation for field transfer in non linear mechanics. *Eur J Comput Mech* 15:571–587
44. Hughes TJ, Cottrell JA, Bazilevs Y (2005) Isogeometric analysis: Cad, finite elements, nurbs, exact geometry and mesh refinement. *Comput Methods Appl Mech Eng* 194:4135–4195

Publisher's Note Springer Nature remains neutral with regard to jurisdictional claims in published maps and institutional affiliations.